



Nuclide identification of radioactive sources from gamma spectra using artificial neural networks

N.P. Barradas^{a,b,*}, A. Vieira^c, M. Felizardo^a, M. Matos^d

^a C2TN, Department of Nuclear Engineering and Sciences, Instituto Superior Técnico, Lisbon University, Portugal

^b Instituto de Plasmas e Fusão Nuclear, Instituto Superior Técnico, Lisbon University, Portugal

^c Medgical.AI, Portugal

^d International Atomic Energy Agency, Austria

ARTICLE INFO

Handling Editor: Dr. Chris Chantler

Keywords:

Gamma spectroscopy
Artificial intelligence
Artificial neural networks
Nuclear security

ABSTRACT

Gamma spectroscopy is commonly used to identify the radionuclides present in samples or materials, by using the existing knowledge on the gamma ray energies and intensities for each radionuclide. However, when dealing with samples where the composition, internal configuration and shielding materials are unknown, as is the case, for instance, in nuclear security applications, the task can become challenging. Furthermore, gamma detection systems in field applications often do not have the high resolution typical of controlled laboratory conditions. In this work, we apply artificial intelligence techniques for automated identification of radioactive sources from gamma spectra obtained with a LaBr₃(Ce) detector with 3.6 % resolution at 662 keV. Combinations of up to 10 sources in each spectrum were used to train and test the artificial neural network developed. We report on the results, which show effective nuclide identification of radioactive sources from gamma spectra using ANNs.

1. Introduction

Gamma ray spectroscopy is a well-established and mature technique for the determination of the energy and intensity of gamma radiation (Buchtele, 2019). It is used for the identification of gamma emitting radionuclides present in samples, and for the quantification of their amount, including for in-situ field applications, detection of artificial radionuclides, nuclear analytical techniques and forensic applications (Martin et al., 2024; Holschuh et al., 2022; Cerezo et al., 2023; Pessoa Barradas et al., 2020; Simon et al., 2022, 2024).

In principle, the analysis of gamma ray spectra for identifying the radionuclides present is a straightforward task, given that the gamma ray energies for each radionuclide are well known. In practice, there are several difficulties when using gamma spectroscopy of unknown samples, where it is a priori unknown how many and which radionuclides are present, and what is the internal configuration of the sample, including possible shielding. This is often the situation in radiological and nuclear security applications (Kouzes, 2005; Runkle et al., 2009). Some of those difficulties are: first, the intensities of gamma ray lines can be very different for the different radionuclides, as mixture of high intensity and low intensity sources is often present in one given sample.

Then, shielding attenuates different gamma rays differently, which affects the intensity of all gamma ray lines, but also affects the line ratio in radionuclides with more than one significant gamma ray. In nuclear security applications, shielding is often unknown, and these attenuations cannot be calculated a priori, which makes theoretical calculation of intensities very challenging. Also, some radionuclides may be near or below the limit of detection (LOD). In cases where all gamma ray intensities of a radionuclide are below the LOD, no software or data analysis procedure can help. When at least one gamma ray is above, albeit near, the LOD, conventional data analysis techniques have difficulties in identifying the given radionuclide in an automated way. Finally, field applications often use low resolution detection systems.

Artificial Neural Networks (ANNs) are particularly suited to the analysis of complex data due to their superior pattern recognition capabilities. We have previously shown how ANNs can be efficiently developed to analyse neutron activation analysis data, which is based on gamma spectroscopy, performing as well as state of the art data analysis methods based on first principles (Pessoa Barradas et al., 2023). Different machine learning methods, including ANNs, have also been applied to gamma spectroscopy (Kamuda et al., 2017; Jinhwan et al., 2019; Bilton et al., 2021; Koo et al., 2021; Pérez-Loureiro and Alexander,

This article is part of a special issue entitled: ISRP-16 published in Radiation Physics and Chemistry.

* Corresponding author. C2TN, Department of Nuclear Engineering and Sciences, Instituto Superior Técnico, Lisbon University, Portugal.

E-mail address: nunoni@ctn.tecnico.ulisboa.pt (N.P. Barradas).

<https://doi.org/10.1016/j.radphyschem.2025.112692>

Received 18 November 2024; Received in revised form 3 March 2025; Accepted 11 March 2025

Available online 13 March 2025

0969-806X/© 2025 The Authors. Published by Elsevier Ltd. This is an open access article under the CC BY license (<http://creativecommons.org/licenses/by/4.0/>).

2022; Bandstra et al., 2023; Harrison et al., 2024; Li et al., 2024; Junhyeok et al., 2023; Suárez-Navarro et al., 2024; Kim et al., 2025). Several of these studies were conducted either using synthetic data without testing on experimental data (Bilton et al., 2021; Bandstra et al., 2023; Harrison et al., 2024), or testing on a very small amount of experimental data (Kamuda et al., 2017; Jinhwan et al., 2019; Li et al., 2024; Junhyeok et al., 2023). Many of the studies were conducted on single sources, i.e., on identification of the one single radionuclide present in each spectrum (Bilton et al., 2021; Koo et al., 2021; Pérez-Loureiro and Alexander, 2022; Bandstra et al., 2023; Harrison et al., 2024; Li et al., 2024). Other studies used sources with either a limited number of radionuclides, or radionuclides that have main gamma peaks with energies well separated from the other radionuclides present (Koo et al., 2021; Kim et al., 2025). The study by Pérez-Loureiro et al. (Pérez-Loureiro and Alexander, 2022) used 1951 experimental single source data sets. The study by Suárez-Navarro et al. (2024) analysed multiple sources with several radionuclides but focused on analysing only one of the radionuclides present. The study by Kim et al. (2025) presented a deep learning analysis considering multiple variables for in situ applications, but did not include shielding, which limits its usefulness for nuclear security applications.

The objective of this work is to build on previous work of application of artificial intelligence to gamma spectroscopy, in particular with a large number of radionuclides present in the spectra, measured with a low resolution detection system in different shielding conditions, and making extensive testing with experimental spectra. In this work, 110 gamma ray spectra were measured, involving combinations of up to 10 different sources with different shielding and different measurement conditions: ^{22}Na , ^{57}Co , ^{60}Co , ^{88}Y , ^{109}Cd , ^{133}Ba , ^{137}Cs , ^{152}Eu , ^{204}Tl , ^{241}Am . Single source spectra were used to generate synthetic data using data augmentation techniques to address the issue of limited sample size. An ANN was trained using the synthetic data, and then applied to the analysis of the experimental multiple-source spectra. We report on the results, which show effective nuclide identification of radioactive sources from complex multi-source gamma spectra using ANNs.

2. Experimental data

The experimental setup consisted of 1.5×1.5 in. $\text{LaBr}_3(\text{Ce})$ scintillation crystal in a hermetically sealed aluminium housing, including a photomultiplier tube, an internal magnetic/light shield, and a 14-pin connector. The detector has been combined with the Osprey®-DTB all-in-one HVPS, preamplifier, and digital MCA. The applied high voltage

was 600 V, the shaping rise time $1 \mu\text{s}$ and the energy range went to 2.6 MeV with 1024 channels. The resolution of the system was 3.6 % at 662 keV (^{137}Cs FWHM). The instrument did not perform as well as a new device as it has been used in numerous applications previously and the scintillation material has a background that includes an intrinsic internal decay from the primordial radioisotope ^{138}La . This setup allowed to imitate more realistic data similar to results that Front Line Officers would obtain instead of sterile laboratory conditions.

Over the duration of 6 months (August 25, 2023–February 14, 2024) 110 spectra have been recorded. Various combinations of following sources have been used (activity on August 25, 2023) ^{204}Tl (6.32×10^4 Bq), ^{137}Cs (5.66×10^5 Bq), ^{60}Co (3.24×10^5 Bq), ^{57}Co (6.43×10^3 Bq), ^{109}Cd (1.11×10^4 Bq), ^{152}Eu (4.08×10^5 Bq), ^{88}Y (4.95×10^2 Bq), ^{241}Am (4.64×10^5 Bq), ^{133}Ba (3.94×10^5 Bq), and ^{22}Na (1.44×10^5 Bq). To match various levels of activities, the sources were placed at several distances, from the source-detector on contact (0 cm) to 10 cm. In several cases we have also used Pb shielding of 2 or 5 mm. The higher thickness was sufficient to attenuate some gamma peaks below LOD.

The background has been recorded regularly. One recorded background spectrum is shown in Fig. 1, with the contributions from several phenomena indicated. These include X-rays, gamma rays and beta rays from the intrinsic decay of the ^{138}La present in the scintillation crystal, alpha particles from the uranium decay chain, and gamma rays from external natural ^{40}K present in the surroundings of the detection system (Alexiev et al., 2008).

The energy calibrations with ^{137}Cs , ^{60}Co , ^{88}Y , and ^{241}Am sources were repeated each month. Small variations in peak positions (up to 2 channels) were observed. The gamma peaks used for the calibrations are shown in Fig. 2, with the corresponding gamma energies identified.

Two examples of spectra used to evaluate the performance of the ANN are shown in Fig. 3. The ANN was able to identify the ^{109}Cd , ^{22}Na , and ^{152}Eu , but failed to find ^{204}Tl . For more discussion, see Chapter 4.

3. Artificial neural networks

3.1. ANN architecture

For this work we used Convolutional Neural Networks (CNNs) (Géron, 2022). CNNs are neural networks specifically designed for processing structured grid data. They are crucial for image processing because they adaptively learn spatial hierarchies of features through backpropagation, significantly enhancing tasks such as object detection, image classification, and segmentation. By leveraging convolutional

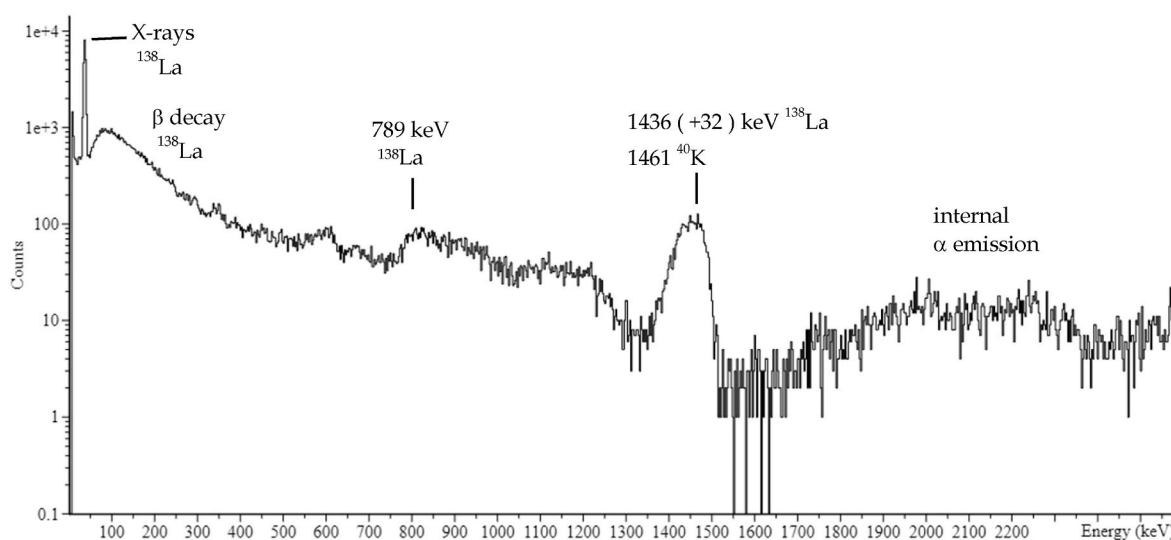


Fig. 1. Background spectrum collected with the $\text{LaBr}_3(\text{Ce})$ scintillation crystal. Intrinsic radiation from ^{138}La (including X-rays, gamma rays and beta rays), internal alpha emission from the uranium decay chain, and external radiation from ^{40}K is also detected.

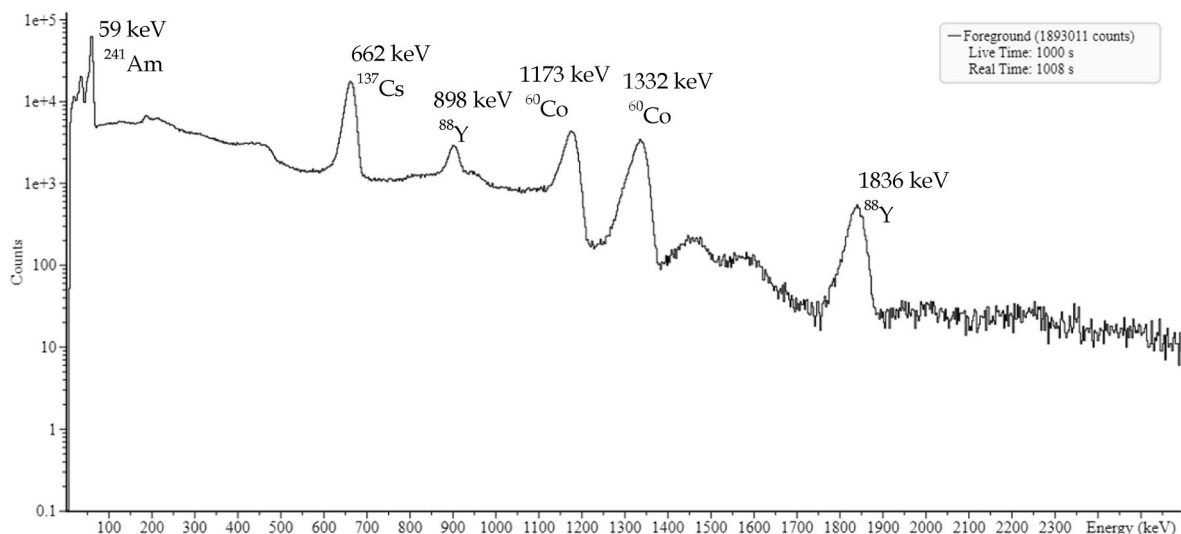


Fig. 2. Energy calibration spectrum collected with the $\text{LaBr}_3(\text{Ce})$ scintillation crystal. ^{137}Cs , ^{60}Co , ^{88}Y , and ^{241}Am sources were used for the calibration. The gamma peaks used are indicated, together with their respective energies.

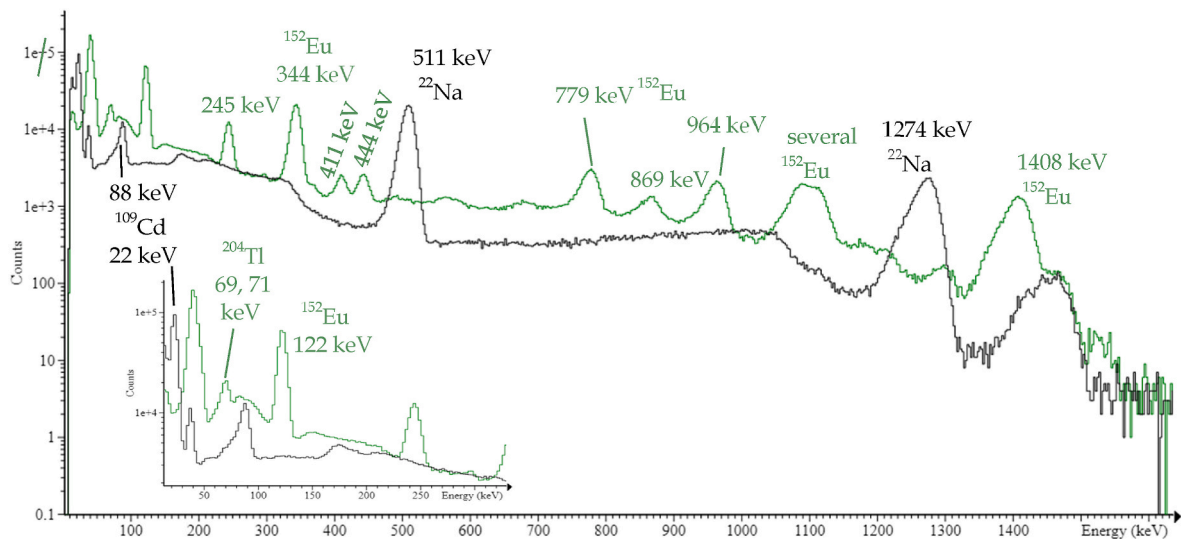


Fig. 3. Two $\text{LaBr}_3(\text{Ce})$ scintillation crystal energy spectra, shown up to 1600 keV. One (black) was collected from ^{109}Cd and ^{22}Na sources and one (green) from ^{204}Tl and ^{152}Eu sources. The gamma ray peaks are identified, together with their respective energies. The insert shows the low energy part of the spectra. (For interpretation of the references to colour in this figure legend, the reader is referred to the Web version of this article.)

layers, CNNs efficiently reduce the dimensionality of images while preserving essential features, leading to highly accurate and robust image analysis. The benefits of using 1D CNNs for Signal Analysis are (Géron, 2022; Kiranyaz et al., 2021):

- 1. Automatic Feature Extraction:** Unlike traditional methods that require manual feature engineering, CNNs automatically learn features from the raw input data.
- 2. Parameter Sharing:** Convolutional layers share parameters (weights) across different positions of the input, making the network more efficient and less prone to overfitting.
- 3. Local Connectivity:** The use of kernels (w) helps in capturing local patterns within the input signal, which is crucial for understanding spectra data.
- 4. Reduction in Computational Complexity:** By using pooling layers, the network reduces the dimensionality of the data, thus lowering the computational complexity, thus improving generalisation.

The convolution operation slides the kernel w across the input x , performing element-wise multiplications and summing them up along with the bias term to produce the output feature map y . In signal analysis, 1D CNNs are particularly effective because they can capture local dependencies and patterns in the data. For instance, in a time-series dataset, patterns such as peaks, trends, and repetitive signals can be efficiently identified through the convolutional layers.

In our case, we fed the spectra (down-sampled to 256 or 512 channels) using up to three 1D convolutional layers followed by max pooling layers to introduce a computational bottleneck (Géron, 2022), as shown in Table 1. To regularise the network, we used L_2 regularization on the dense layers. L_2 regularization is a technique used in training neural networks to prevent overfitting, which occurs when a model performs well on training data but poorly on unseen data. It works by adding a penalty term to the loss function, which discourages the network from fitting the noise in the training data too closely - penalises large weights.

As loss function we used a weighted binary cross-entropy (Géron, 2022), that is the most suitable for classification problems, given by the

Table 1
ANN architecture.

Layer (type)	Output Shape	Parameters
input_c(InputLayer)	(None,256,1)	0
conv1d_1(Conv1D)	(None,252,100)	600
max_pooling1d_1	(None,126,100)	0
flatten_1(Flatten)	(None,3050)	0
layer2(Dense)	(None,30)	91530
layer_out(Dense)	(None,10)	310

Total number of parameters: 117490 (458.95 KB).

expression:

$$BCE = -\frac{1}{N} \sum_{i=1}^N w_i \left(y_{true,i} \log(y_{pred,i}) + (1 - y_{true,i}) \cdot \log(1 - y_{pred,i}) \right)$$

where y_{pred} are predictions and y_{true} are the real labels. The sum is on the number N of radionuclides. The weights w_i are intended to allow for the possibility to give more weight in the training to certain radionuclides, a technique common in deep learning architectures (Rengasamy et al., 2020; van der Meer et al., 2022). By default, they are all equal to 1, corresponding to equal weight to all radionuclides. The following describes the architecture of one kind of network tested. It is composed of a 1-dimensional convolutional layer (conv_1d) followed by a flatten layer (flatten_1), a dense layer with 30 neurons with the *gelu* activation function. Finally, the output layer (layer_out) consists of 10 neurons (one for each nuclide) using a sigmoid activation.

We used Tensorflow Keras framework to build and train the network using the Adam optimizer (Kingma and Ba, 2015). We trained the network using 50 thousand synthetic spectra. From these examples, a random sample of 80 % was used for the train set, i.e. these synthetic spectra were presented to the ANN with known outputs, and the remaining 20 % were used for the test set, which are not directly used to train the ANN. Training was set to run up to 50 epochs or when the loss in the test set reaches an absolute minimum (see Fig. 4). Note that the output of the network are continuous values (from 0 to 1). To decide if a nuclide is present in the sample or not, we need to set a detection threshold level - in this case we took the obvious choice of 0.5. This threshold can be varied depending on the trade-off required between specificity and sensitivity (Rainio et al., 2024; Cheng et al., 2022). Since a few elements were hardest to detect, i.e. ^{57}Co , ^{109}Cd , ^{204}Tl , and ^{241}Am , we gave a higher weight to these radionuclides in the weighted loss

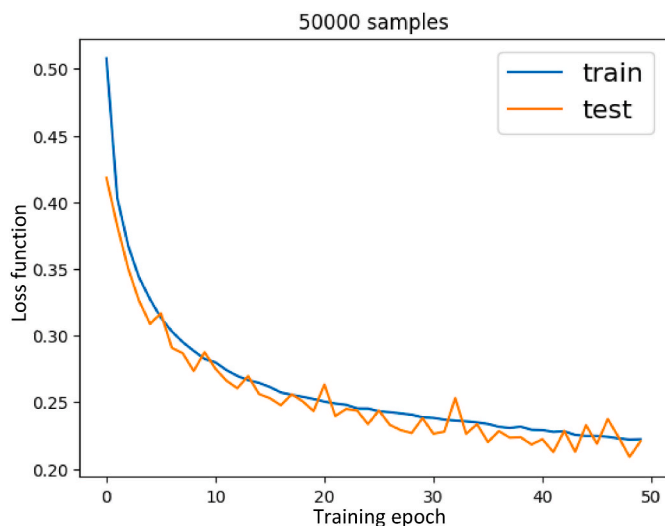


Fig. 4. Loss function for the train and test sets during training. In this case, 50000 synthetic spectra were used in the training, randomly divided in 80 % for the train set and 20 % for the test set.

function, to put more emphasis in these radionuclides.

3.2. Synthetic data

ANNs usually require a large amount of training data. In the present problem, with a large number of inputs (the number of channels) and ten different outputs, the resulting ANNs have a very large number of connections and parameters, and the requirements for number of training data are consequently also very large. ANNs trained with limited amounts of data are prone to over-training, i.e., becoming specialized for the data they have been trained with, with limited capability of generalization to other cases. It is not feasible to measure a sufficient number of experimental spectra to train the ANN. Different approaches have been previously developed to tackle this issue. One approach, to use theoretically calculated data, has been used for techniques such as Rutherford backscattering (Barradas and Vieira, 2000; Demeulemeester et al., 2013), elastic backscattering (Vieira and Barradas, 2001), elastic recoil detection analysis (Nené et al., 2006), prompt gamma activation analysis (Bilton et al., 2021), and gamma spectroscopy (Harrison et al., 2024). It has the advantage that any number of data, for any given experimental parameters, can be generated. One drawback is that the calculations can be very time-consuming, limiting the number of synthetic data that can be generated. Another potential drawback is that, if the theoretical calculation is not sufficiently realistic and accurate, the ANN will not be able to correctly analyse the experimental data. Another approach is to use a limited number of experimental data to generate synthetic data. This was successfully used in neutron activation analysis (Pessoa Barradas et al., 2023), which is also based on gamma spectroscopy, and was the option taken in this work.

Synthetic data were generated by linear combination of experimental data, after due consideration to pulse pileup was given. Pulse pileup is non-linear, and does not simply add when two sources are combined. In other words, the pileup resulting from two sources being measured simultaneously is not equal (and in fact can be very different) to the sum of the pileup resulting from each source being measured separately. We addressed this by the following procedure: first, we used the algorithm by Barradas and Reis (2006) to calculate the pileup in the experimental data. The algorithm depends on a few parameters, which were determined by analysing three experimental spectra measured explicitly for this purpose. These were from high activity sources at zero distance to the detector: ^{60}Co and ^{137}Cs first measured separately, and then measured together.

Fig. 5 illustrates the pileup calculation, showing the raw data, the corresponding calculated pileup, and the data after subtraction of the calculated pileup (from now called “pileup-subtracted”) for individual ^{137}Cs and ^{60}Co sources measured separately, and for the two sources measured together, always in the same experimental conditions (sources at 0 cm from the detector, no shielding). For the ^{60}Co source, the pileup of the 1.173 MeV line (marked as Co_1 in the figure) with itself is observed (channel 966). The pileup of the 1.173 MeV line with the 1.332 MeV (marked as Co_2 in the figure) is partially observed (the peak would be at channel 1030, so only its left-hand side is seen) while the pileup of Co_2 with itself is not observed, as the measurement only extends to 2.475 MeV. For the ^{137}Cs source, the pileup of the 0.6617 MeV line (marked as Cs_1 in the figure) with itself is observed (channel 548). It is very well reproduced by the calculation, with the remainder peak area being two order of magnitudes lower. A small inaccuracy in the energy calibration leads to a small shift between the calculated and observed signals. The very small triple pileup signal at channel 822 is only partially reproduced, which shows the limits of the pileup calculation algorithm. It is noted that the double pileup peak has an energy close to that of the 1.332 MeV ^{60}Co line, in practice indistinguishable when measured with low resolution systems. In spectra where another spurious signal would be present near the 1.173 MeV ^{60}Co line, a false positive for ^{60}Co could be triggered if pileup was not properly considered. Finally, for the combined ^{137}Cs and ^{60}Co sources, the pileup of the

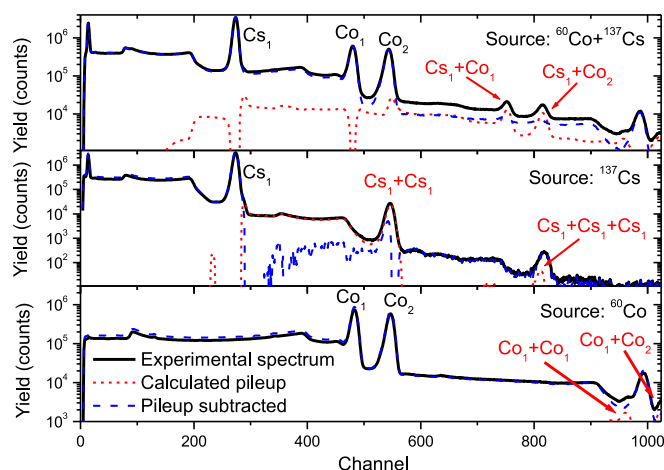


Fig. 5. Illustration of the pileup calculation for single radionuclide sources and for a source with two radionuclides present. The solid black lines show the spectra obtained from measuring ^{137}Cs and ^{60}Co single sources, and a source with both radionuclides. The short-dashed red lines show the calculated pileup. The dashed blue lines show the measured spectrum after subtraction of the calculation pileup. (For interpretation of the references to colour in this figure legend, the reader is referred to the Web version of this article.)

^{137}Cs line with the ^{60}Co lines is observed and well reproduced. Again, without including pileup in the analysis, these lines could lead to false positives of radionuclides that emit gamma rays with similar energies.

Then, the pileup was calculated for all other experimental data, which have lower count rate and hence also lower pileup. We subtracted the calculated pileup from the experimental data, obtaining pileup-subtracted spectra. It is these pileup-subtracted spectra that were combined linearly to form the synthetic data, which are therefore pileup-free. The last step was to add calculated pileup to the synthetic data, leading to realistic spectra. Fig. 6 illustrates the process of generating a

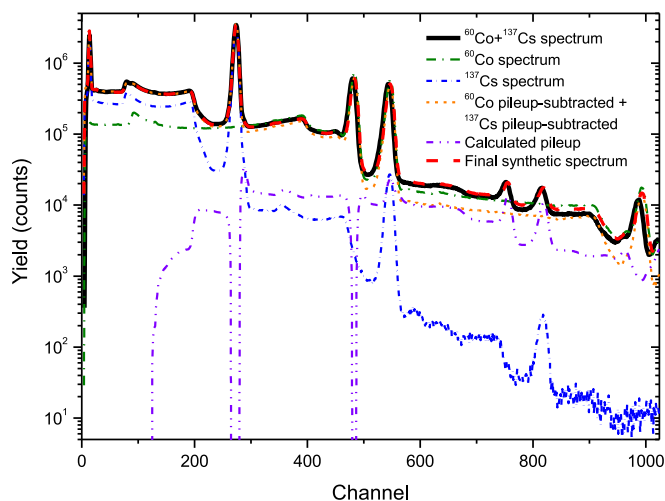


Fig. 6. Illustration of the steps involved in the pileup calculation. The solid black line shows the experimental spectrum obtained from measuring a combined ^{137}Cs and ^{60}Co source. The dash-dotted green line and the short dashed blue line are the spectra from individual ^{137}Cs and ^{60}Co sources, respectively. The short-dashed orange line is obtained by linear combination of the individual pileup-subtracted ^{137}Cs and ^{60}Co spectra. The dash-dot-dotted violet line shows the calculated pileup. The dashed red line shows the final synthetic spectrum for the combined ^{137}Cs and ^{60}Co source, which closely matches the experimental spectrum. (For interpretation of the references to colour in this figure legend, the reader is referred to the Web version of this article.)

synthetic spectrum based on single source experimental spectra, for the case of a combined ^{137}Cs and ^{60}Co source. A weighted average of the single source pileup-subtracted spectra was made, using weights chosen to reproduce the main ^{137}Cs and ^{60}Co line intensities of the combined ^{137}Cs and ^{60}Co source. The result is a pileup-free combined ^{137}Cs and ^{60}Co spectrum. The following step is to add calculated pileup, leading to a synthetic spectrum which is very similar to the measured spectrum.

A restricted number of experimental data was selected to generate the synthetic data: only the 27 single source experimental data collected with the same live time (1000 s) were used. This is not a principled restriction, and the code gives the user the option to use experimental data collected with more sources and with different live time values. We call this set of 27 experimental data the “experimental training set”. For each synthetic spectrum, a random number of spectra from the experimental training set was selected, from a minimum of 1 to a maximum of 10 for 40 % of the synthetic spectra, and a maximum of 27 for the remainder. A (logarithmic) random factor from 10^{-2} to 10^2 was used as multiplicative weight for each of the experimental spectra. A further (logarithmic) random factor from 10^{-2} to 10^2 was used as multiplicative weight for the total yield with respect to the average yield of the selected experimental spectra. Additionally, 1 % of the synthetic spectra were generated from background experimental spectra, collected without sources.

In this process, it is possible that a radionuclide that is visible above the LOD in the original single source experimental spectrum, becomes invisible (i.e., below LOD) in the synthetic spectrum, because it is superimposed to a large background or a large peak coming from a different radionuclide from one of the other original single source experimental spectra used to construct the synthetic spectrum. The code for generation of synthetic data checks, for each radionuclide in principle present, whether at least one of the respective gamma lines is above the LOD (Alvarez, 2007). If not, the radionuclide is considered not to be present in the synthetic spectrum.

The experimental data had 1024 channels. This is a high number of inputs for an ANN, which leads to a very high number of parameters and, consequently, to difficulties in training the ANN efficiently and increases the risk of overfitting. In order to reduce the number of parameters, we compressed the synthetic spectra by grouping every four or every two channels thus reducing the number of channels to 256 or 512, respectively. The latter case, 512 channels, leads to an energy width of the compressed channels close to the FWHM energy resolution of the detector used, which should be sufficient to discriminate between neighbouring gamma lines in most cases.

4. Results and discussion

Once trained, the ANN was applied to the 70 experimental spectra with two or more radionuclides present and acquisition time 1000 s, which we call the performance set. We used two metrics to evaluate the performance of the ANN: False Positives (FP), which is the number of cases predicted as present when they are in fact absent, and False Negatives (FN), which is the number of cases predicted as not present when they are present in the sample.

We also used the automatic peak recognition routine of the InterSpec spectral radiation analysis software (Johnson et al., 2021) in order to ascertain how well the performance of the ANN compares with that of traditional peak recognition methods. With InterSpec we can only calculate FNs, i.e., instances when the software could not recognize any of the lines correspondent to a radionuclide which was present in the sample. We considered that, for radionuclides with more than one line, recognition of a single line was sufficient as identification of the radionuclide as present. Finally, we note that automatic peak recognition is usually just a first step in human analysis of gamma ray spectra, followed by interactive software-aided analysis by an experienced analyst.

The results are given in Table 2. The number of total positives and total negatives in the performance set are also shown. For instance, 25

Table 2

Results of ANN compared with Interspec software (IS) for the 70 samples of the performance set. The “true” FP and FN take into account the information actually present in spectra (see text for further explanation).

Radionuclide	Total positives in set	Total negatives in set	FP (ANN)	FN (ANN)	FN (IS)	“True” FP (ANN)	“True” FN (ANN)
Co-60	25	45	0	0	0	0	0
Cs-137	26	44	0	0	0	0	0
Am-241	18	52	0	6	7	0	0
Y-88	21	49	0	4	4	0	0
Eu-152	21	49	1	0	0	1	0
Ba-133	15	55	0	0	0	0	0
Na-22	11	59	0	0	0	0	0
Co-57	11	59	4	4	4	4	3
Tl-204	10	60	4	3	3	4	1
Cd-109	29	41	2	13	16	0	1

out of 70 spectra in the performance set had Co-60 present.

A first observation is that the ANN correctly identifies all spectra where Co-60, Cs-137, Eu-152, Ba-133 and Na-22 are present, with no FN results. For the other radionuclides, some FN results are obtained, from three for Tl-204 to 13 for Cd-109. This might indicate a poor performance of the ANN. However, a first indication that this is not the case is that the ANN performs as well as, and in some cases even slightly better than, the automatic peak recognition routine of InterSpec.

We therefore inspected visually all spectra where FNs were obtained by the ANN. As an example, the FN spectra for Y-88 are shown in Fig. 7, where the Y-88 and Eu-152 single source spectra are also shown for reference. In all the cases where FNs were obtained for Y-88, Eu-152 was also present, with an intensity much higher than that of the Y-88 source. As a consequence, the Y-88 peaks are actually not visible, i.e. they are below LOD in these four spectra. The ANN negative predictions reflect this fact (and InterSpec also does not recognize the presence of Y-88 in the same four spectra), and are wholly correct for the data as given: no software can recognize the presence of a radionuclide when its signal is below the LOD.

A similar analysis for the other FNs shows that, for Am-241 all FN results are correct (i.e. the peaks are below LOD), and that for Co-57, Tl-204 and Cd-109, respectively only three, one and one FN results, are actual ANN mistakes, where the radionuclides might have been correctly identified. The Co-57 case is shown in Fig. 8, where the four spectra where the ANN reported FNs are shown, as well as the single source Co-57, which is shown as reference. It is clear that only in one of the four FN results there is no visible Co-57 peak. In the other three

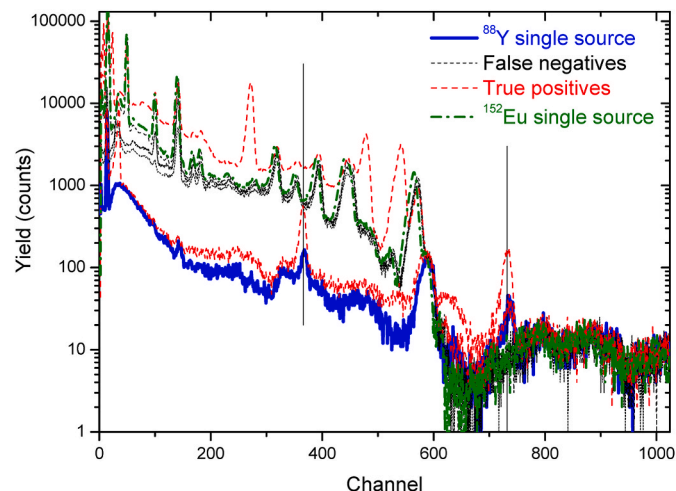


Fig. 7. FNs obtained by the ANN for Y-88. The Y-88 and Eu-152 single source spectra are also shown, for reference. Two examples of true positives, i.e. cases in which the ANN correctly identified that Y-88 was present, are also shown. The vertical lines indicate the position of the 0.898 and 1.836 MeV lines of Y-88.

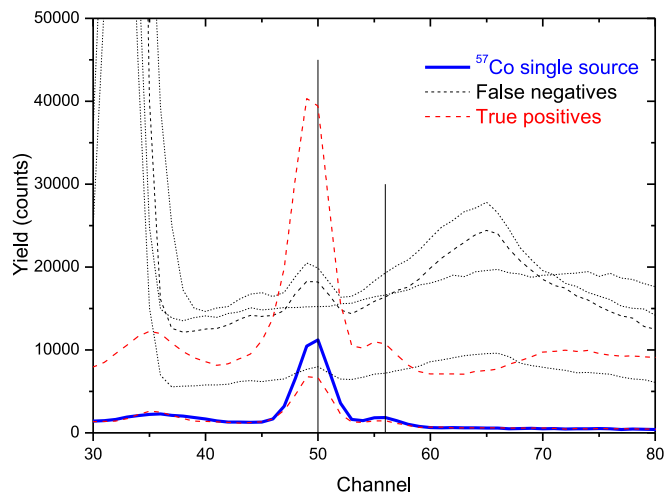


Fig. 8. FNs obtained by the ANN for Co-57. The Co-57 single source spectrum is also shown, for reference. Two examples of true positives, i.e. cases in which the ANN correctly identified that Co-57 was present, are also shown. The vertical lines indicate the position of the 0.122 and 0.136 MeV lines of Co-57.

cases, the 0.122 MeV peak is visible, albeit with rather poor signal to background ratio. It is noted that, albeit the automatic peak recognition routine of InterSpec also failed in these three cases, an experienced human analyst might be able to identify the presence of Co-57, particularly if this was seen a priori as a possibility. As it is, we speculate that including spectra with worse signal to background ratio in the training set, for instance relaxing the LOD criterium used (Alvarez, 2007), might lead to an ANN that is better trained to identify signals close to the LOD. This will be the object of future work.

For Cd-109, the very large number of FNs corresponds in nearly all cases to spectra where Ba-133 is also present, with very intense signal in the region of the Cd-109 peaks, making the latter effectively always below LOD. The one exception is one spectrum where Ba-133 was not present, and where better sensitivity to cases with poor signal to background ratio, as discussed above for Co-57, might help.

The situation for FPs, obtained for Eu-152, Co-57, Tl-204 and Cd-109, is more complex. All four instances for Tl-204 seem to be random errors of the ANN, as there are no signal superpositions or evidence of any peak that could be attributed to Tl-204. The same is true for the FP obtained for Eu-152. One possibility to explain this could be bias in the training data, which contains very few negative examples (only 1 % of spectra in the training set) with background only. This imbalance may cause the ANN to be overly sensitive to potential positive results, increasing the likelihood of occurrence of FPs.

However, this is not the only situation. The FPs for Co-57 are shown in Fig. 9, where the Co-57 and Eu-152 single source spectra are also shown for reference. In all cases Eu-152 was also present, with a strong

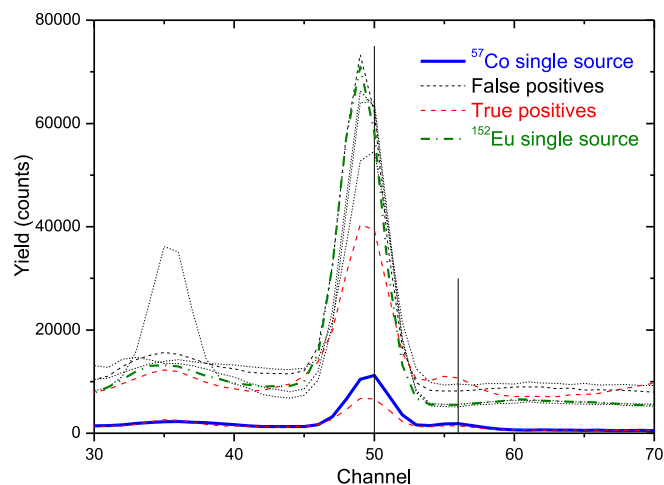


Fig. 9. FPs obtained by the ANN for Co-57. The Co-57 and Eu-152 single source spectra are also shown, for reference. Two examples of true positives, i.e. cases in which the ANN correctly identified that Co-57 was present, are also shown. The vertical lines indicate the position of the 0.122 and 0.136 MeV lines of Co-57.

signal very close the Co-57 peak. A high resolution detection system might be capable of resolving the two lines, but the purpose of the present paper is to present results for low resolution detection typical of field work. Here, the origin of the FPs seems to be the criterium adopted in the code, where detection of a single line corresponding to a radionuclide is sufficient for a positive identification. In fact, in the four FP spectra for Co-57, the 0.122 MeV line is so intense that the 0.136 MeV line would also necessarily be observed, if Co-57 was indeed present. An experienced human analyst would likely recognize this fact and dismiss the FP as a spurious result. One possibility for future work is to automate this criterion and include it in the algorithm: if one line is present above LOD, other lines of the same radionuclide would be checked. If they would also be above LOD, but are not observed in the spectrum, then the algorithm would recognize it is a FP. However, it must be noted that this only works for lines with energy not too far apart, because the line intensity ratios are changed by any shielding, which is not known a priori

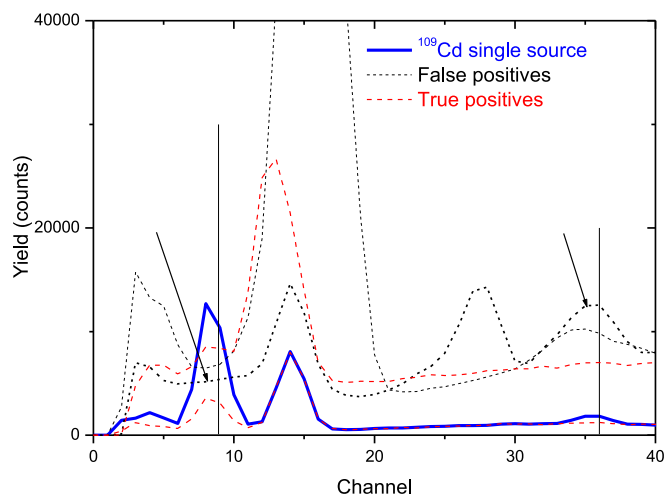


Fig. 10. FPs obtained by the ANN for Cd-109. The Cd-109 single source spectrum is also shown, for reference. Two examples of true positives, i.e. cases in which the ANN correctly identified that Cd-109 was present, are also shown. The vertical lines indicate the position of the 0.022 MeV X ray line and 0.088 MeV gamma ray line of Cd-109. The arrows indicate the same particular FP spectrum.

in sources inside unknown containers. This is illustrated in Fig. 10 for Cd-109, where a large signal is observed near the 0.088 MeV gamma ray line of Cd-109 for the FP spectrum indicated by two arrows. The absence of a peak near the 0.022 MeV X ray line of Cd-109 could be due to shielding absorbing more the lower energy. That is to say, from the spectrum alone, and not knowing which shielding is present, it is not possible to rule out the presence of Cd-109.

The considerations above for FN and FP results lead us to revise what can actually be considered as a “true” FN and a “true” FP result: these are those cases where, from the data alone, the ANN actually committed an error, i.e. there was information present in the spectrum that would have allowed correct identification of the presence or not of the given radionuclide. These “true” FP and FN are given as the rightmost columns in Table 2.

5. Conclusions

We developed an ANN for identification of radionuclides in unknown sources, involving combinations of up to 10 different sources: ^{22}Na , ^{57}Co , ^{60}Co , ^{88}Y , ^{109}Cd , ^{133}Ba , ^{137}Cs , ^{152}Eu , ^{204}Tl , ^{241}Am . The key for successful implementation is the ability to generate high quality synthetic spectra in numbers sufficient to train a complex ANN. The synthetic data were based on linear combinations of single source experimental spectra, with proper consideration of pileup effects allowing for the generation of realistic spectra.

The resulting ANN was applied to 70 multi-radionuclide experimental spectra which had not been used to generate the synthetic data or to train the ANN. The results were excellent: on the one hand, the ANN performed better than conventional automatic methods based on peak recognition software. On the other hand, the number of cases where the ANN wrongly predicted the presence or absence of a given radionuclide was very low, once it is considered whether there is information sufficient in the experimental data to conclude whether the radionuclide can be detected above the LOD.

FN results are detrimental, in that they can give field staff wrong information on the absence of a given radionuclide in a measured sample. Positive results can be flagged by the software to be further checked by field staff. However, a high FP rate can lead to staff losing confidence in the system, which would jeopardise its effectiveness, as staff might feel encouraged to not follow up on reported positive results. Possibilities to improve the results further were discussed in the paper, to reduce the rate of both FPs and FNs. Also, it is possible to develop further the ANN to provide confidence limits on the positive results reported. This can be done, e.g., by including the LOD in the reported outputs, or by outputting a range of ANN quantitative outputs, for instance from 0 (not present) to 10 (high confidence), instead of 0/1 (no/yes). We plan to develop such confidence metrics in future work.

Another method to improve accuracy would be to include more than one spectrum as input, for instance in situations where more than one detector is used. We have previously used this strategy in other nuclear analytical techniques with excellent results (Nené et al., 2006; Pinho et al., 2005).

In future work, we also plan to expand the experimental data set to extend the methodology to include further radionuclides of interest to nuclear security and safeguards, such as uranium isotopes and plutonium.

CRediT authorship contribution statement

N.P. Barradas: Writing – review & editing, Writing – original draft, Software, Methodology, Formal analysis, Data curation, Conceptualization. **A. Vieira:** Writing – review & editing, Writing – original draft, Software, Methodology, Formal analysis, Data curation. **M. Felizardo:** Writing – review & editing, Validation. **M. Matos:** Writing – review & editing, Writing – original draft, Resources, Methodology, Investigation, Funding acquisition, Data curation, Conceptualization.

Declaration of competing interest

The authors declare that they have no known competing financial interests or personal relationships that could have appeared to influence the work reported in this paper.

Funding Acknowledgement

Received funding from IAEA Contract TAL-NSNS20231117-005, Nuclide identification of shielded radioactive sources from measured spectra using artificial neural networks.

Data availability

Data will be made available on request.

References

- Alexiev, D., Mo, L., Prokopovich, D., Smith, M., Matuchova, M., 2008. Comparison of LaBr₃:Ce and LaCl₃:Ce with NaI(Tl) and cadmium zinc telluride (CZT) detectors. *IEEE Trans. Nucl. Sci.* 55, 1174–1177. <https://doi.org/10.1109/TNS.2008.922837>.
- Alvarez, J.L., 2007. Poisson-based detection limit and signal confidence intervals for few total counts. *Health Phys.* 93, 120–126. <https://doi.org/10.1097/01.hp.0000261331.73389.bd>.
- Bandstra, M.S., et al., 2023. Explaining machine-learning models for gamma-ray detection and identification. *PLoS One* 18, e02868292023. <https://doi.org/10.1371/journal.pone.0286829>.
- Barradas, N.P., Reis, M., 2006. Accurate calculation of pileup effects in PIXE spectra from first principles. *X Ray Spectrom.* 35, 232–237. <https://doi.org/10.1002/XRS.903>.
- Barradas, N.P., Vieira, A., 2000. Artificial neural network algorithm for analysis of Rutherford backscattering data. *Phys. Rev. E* 62, 5818–5829. <https://doi.org/10.1103/PhysRevE.62.5818>.
- Bilton, K.J., et al., 2021. Neural network approaches for mobile spectroscopic gamma-ray source detection. *J. Nucl. Eng.* 2, 190–206. <https://doi.org/10.3390/jne2020018>.
- Buchtela, K., 2019. Radiochemical Methods|Gamma-ray spectrometry. In: *Encyclopedia of Analytical Science*, third ed., pp. 15–22. <https://doi.org/10.1016/B978-0-12-409547-2.11333-2>.
- Cerezo, A., Prieto, E., Reichardt, I., Casanovas, R., Salvadó, M., 2023. A fast algorithm for real-time monitoring of artificial radioisotopes in presence of variable natural radioactivity. *Radiat. Phys. Chem.* 209, 110946. <https://doi.org/10.1016/j.radphyschem.2023.110946>.
- Cheng, X., Han, X., Song, Y., Zhang, T., Xu, B., 2022. Artificial neural network-assisted amplitude thresholding improves spike detection. *Proc. ICCPR 2022: 2022 11th International Conference on Computing and Pattern Recognition (ICCP)*, pp. 465–470. <https://doi.org/10.1145/3581807.3581875>. Beijing, China.
- Demeulemeester, J., et al., 2013. On the growth kinetics of Ni(Pt) silicide thin films. *J. Appl. Phys.* 113, 163504. <https://doi.org/10.1063/1.4802738>.
- Géron, A., 2022. *Hands-On Machine Learning with Scikit-Learn, Keras, and TensorFlow*, second ed. O'Reilly Media. ISBN 9781492032649.
- Harrison, G., et al., 2024. Modelling tools for enhancing nuclear security. *Proc. ICONS 2024, International Conference on Nuclear Security: Shaping the Future*. Vienna, Austria (preprint).
- Holschuh, T.V., Ocampo Giraldo, L.A., Snow, M.S., Chichester, D.L., 2022. Gamma-ray spectrometry analysis methods for radioisotope dissolution and mixing for nuclear forensics applications. *J. Radioanal. Nucl. Chem.* 331, 5231–5236. <https://doi.org/10.1007/s10967-022-08462-3>.
- Jinhwan, K., et al., 2019. Quantitative analysis of NaI(Tl) gamma-ray spectrometry using an artificial neural network. *Nucl. Instrum. Methods Phys. Res., Sect. A* 944, 162549. <https://doi.org/10.1016/j.nima.2019.162549>.
- Johnson, W., Chan, E., Walsh, E., Morte, C., Lee, D., 2021. InterSpec v. 1.0.8. Computer software. <https://github.com/sandialabs/InterSpec.USDOE>. <https://doi.org/10.1157/dc.20211202.6>.
- Junhyeok, K., et al., 2023. Untrained neural network-based unfolding method for quantitative analysis of NaI(Tl) gamma spectrometers. *Radiat. Phys. Chem.* 209, 110993. <https://doi.org/10.1016/j.radphyschem.2023.110993>.
- Kamuda, M., Stinnett, J., Sullivan, C.J., 2017. Automated isotope identification algorithm using artificial neural networks. *IEEE Trans. Nucl. Sci.* 64, 1858–1864. <https://doi.org/10.1109/TNS.2017.2693152>.
- Kim, W., et al., 2025. Deep learning-based gamma spectroscopic analysis considering multiple variables for in situ applications. *Radiat. Phys. Chem.* 226, 112261. <https://doi.org/10.1016/j.radphyschem.2024.112261>.
- Kingma, D., Ba, J., 2015. Adam: a method for stochastic optimization. *Proc. International Conference on Learning Representations. ICLR*, San Diego, CA, USA. <https://doi.org/10.48550/arXiv.1412.6980>.
- Kiranyaz, S., et al., 2021. 1D convolutional neural networks and applications: a survey. *Mech. Syst. Signal Process.* 151, 107398. <https://doi.org/10.1016/j.ymsp.2020.107398>.
- Koo, B.T., et al., 2021. Development of a radionuclide identification algorithm based on a convolutional neural network for radiation portal monitoring system. *Radiat. Phys. Chem.* 180, 109300. <https://doi.org/10.1016/j.radphyschem.2020.109300>.
- Kouzes, R., 2005. Detecting illicit nuclear materials. *Am. Sci.* 93, 422. <https://doi.org/10.1511/2005.55.422>.
- Li, J., Alexander, J., Echlin, M., Stoev, K., Thompson, M., 2024. Advancing isotope identification algorithms for mid-resolution detectors. *Proc. ICONS 2024, International Conference on Nuclear Security: Shaping the Future*. Vienna, Austria (preprint).
- Martin, L., Duval, M., Arnold, L.J., 2024. To what extent do field conditions affect gamma dose rate determination using portable gamma spectrometry? *Radiat. Phys. Chem.* 216, 111365. <https://doi.org/10.1016/j.radphyschem.2023.111365>.
- Nené, N.R., Vieira, A., Barradas, N.P., 2006. Artificial neural network analysis of RBS and ERDA spectra of multilayered multielemental samples. *Nucl. Instrum. Methods Phys. Res. B* 246, 471–478. <https://doi.org/10.1016/j.nimb.2006.01.016>.
- Pérez-Loureiro, D., Alexander, J., 2022. Radioisotope identification using CLYC detectors. *Proc. 21st IEEE International Conference on Machine Learning and Applications (Nassau, Bahamas)*, pp. 1358–1364. <https://doi.org/10.1109/ICMLA55696.2022.00214>.
- Pessoa Barradas, N., et al., 2020. International atomic energy agency inter-comparison of particle induced gamma-ray emission codes for bulk samples. *Nucl. Instrum. Methods B* 468, 37–47. <https://doi.org/10.1016/j.nimb.2020.02.019>.
- Pessoa Barradas, N., Farjallah, N., Vieira, A., Blaauw, M., 2023. Artificial neural networks for NAA: proof of concept on data analysed with k0-based software. *J. Radioanal. Nucl. Chem.* 332, 3421–3429. <https://doi.org/10.1007/s10967-022-08568-8>.
- Pinho, H.F.R., Vieira, A., Nené, N.R., Barradas, N.P., 2005. Artificial neural network analysis of multiple IBA spectra. *Nucl. Instrum. Methods Phys. Res. B* 228, 383–387. <https://doi.org/10.1016/j.nimb.2004.10.075>.
- Rainio, O., et al., 2024. Comparison of thresholds for a convolutional neural network classifying medical images. *Int. J. Data Sci. Anal.* <https://doi.org/10.1007/s41060-024-00584-z>.
- Rengasamy, D., Jafari, M., Rothwell, B., Chen, X., Figueredo, G.P., 2020. Deep learning with dynamically weighted loss function for sensor-based prognostics and health management. *Sensors* 23, 723. <https://doi.org/10.3390/s20030723>.
- Runkle, R.C., Smith, L.E., Peurrung, A.J., 2009. The photon haystack and emerging radiation detection technology. *J. Appl. Phys.* 106, 041101. <https://doi.org/10.1063/1.3207769>.
- Simon, A., Pessoa Barradas, N., Romolo, F.S., 2022. Fostering the use of nuclear analytical techniques for forensic science. *Forensic Sci. Int.* 341, 111517. <https://doi.org/10.1016/j.forsciint.2022.111517>.
- Simon, A., Pessoa Barradas, N., Jaynes, C., Romolo, F.S., 2024. Addressing forensic science challenges with nuclear analytical techniques – a review. *Forensic Sci. Int.* 358, 111767. <https://doi.org/10.1016/j.forsciint.2023.111767>.
- Suárez-Navarro, J.A., et al., 2024. ²²⁶Ra activity concentration determined directly from the 186 keV photopeak using gamma spectrometry and a neural network. *Radiat. Phys. Chem.* 217, 111486. <https://doi.org/10.1016/j.radphyschem.2023.111486>.
- van der Meer, R., Oosterlee, C.W., Borovykh, A., 2022. Optimally weighted loss functions for solving PDEs with Neural Networks. *J. Comput. Appl. Math.* 405, 113887. <https://doi.org/10.1016/j.cam.2021.113887>.
- Vieira, A., Barradas, N.P., 2001. Composition of NiTaC films on Si using neural networks analysis of elastic backscattering data. *Nucl. Instrum. Methods Phys. Res. B* 174, 367–372. [https://doi.org/10.1016/S0168-583X\(00\)00621-2](https://doi.org/10.1016/S0168-583X(00)00621-2).